Available online at www.sciencedirect.com
ScienceDirect
International Journal of Heat and Mass Transfer 50 (2007) 4513–4526
International Journal of HEAT and MASS TRANSFER
www.elsevier.com/locate/ijhmt

Local measurement of flow boiling in structured surface microchannels

C.-J. Kuo, Y. Peles *

Department of Mechanical, Aerospace and Nuclear Engineering, Rensselaer Polytechnic Institute, Troy, NY 12180, USA

Received 29 September 2006; received in revised form 19 March 2007
Available online 26 June 2007

Abstract

Experiments were conducted to investigate flow boiling in 200 μm × 253 μm parallel microchannels with structured reentrant cavities. Flow morphologies, boiling inceptions, heat transfer coefficients, and critical heat fluxes were obtained and studied for mass velocities ranging from $G = 83$ kg/m^2 s to $G = 303$ kg/m^2 s and heat fluxes up to 643 W/cm^2. Comparisons of the performance of the enhanced and plain-wall microchannels were performed. The microchannels with reentrant cavities were shown to promote nucleation of bubbles and to support significantly better reproducibility and uniformity of bubble generation. The structured surface was also shown to significantly reduce the boiling inception and to enhance the critical heat flux.

Keywords: Enhanced heat transfer; Boiling; Microchannel; CHF

1. Introduction

Boiling enhancement technique has been a topic of great interest over the last 50 years [1–8], and is a rich field of current study. Of particular engineering success are special heat transfer surfaces encompassing reentrant cavities that promote bubble ebullitions [9–13]. Key engineering system performance parameters that are being enhanced typically include onset of nucleate boiling (ONB), two-phase heat transfer coefficient, and critical heat flux (CHF). Stable structured reentrant cavities were shown to be effective in reducing ONB by an order of magnitude, increasing up to twofold the heat transfer coefficient, and increasing the CHF [11,12]. However, the heat transfer enhancement capabilities strongly depend on the thermal and hydrodynamic conditions as well as the type of structured surface. While some surfaces are more effective in reducing the ONB and increasing the heat transfer coefficient at low mass qualities, others are more effective in increasing the CHF. The enhanced performance is evidently linked to the heat transfer mechanism promoted by these special structured cavities. Several discrete boiling modes from these surfaces have been proposed [14–16], namely, the flooded mode, the suction–evaporation mode, and the dried-up mode. In reality, more than one mode might be triggered in a given structured surface depending on the thermo-hydraulic conditions. The conditions linked to the dominant mode and heat transfer mechanism are generally not well understood [16].

Inspired by the rapid development of boiling in micro-domains [17–21], research endeavors aimed at exploiting recent advances in microfabrication technologies to form structured surfaces that enhance heat transfer for flow/pool boiling are currently underway [22–30]. Honda et al. [22–25] used heat sink with 10–50 μm micro-pin-fins to enhance pool boiling heat transfer, and obtained a reduction in ONB of about 40% and an increase in CHF of up to 2.3 times. Koşar et al. [27,28], Kuo et al. [29], and Pate et al. [30] studied the thermal performance and flow boiling patterns in interconnected reentrant cavities microchannel heat sink. Their results suggest that proper modification of surface topography can provide superior means to manipulate the boiling process. Much is still

* Corresponding author. Tel.: +1 518 276 2886; fax: +1 518 276 2623.
E-mail address: pelesy@rpi.edu (Y. Peles).

0017-9310/$ - see front matter © 2007 Elsevier Ltd. All rights reserved.
doi:10.1016/j.ijheatmasstransfer.2007.03.047

Nomenclature

A_p	platform area (heating surface area above the heater) (m^2)
A_s	total channel cross section area (m^2)
A_t	total channel surface area (m^2)
D_c	size of active nucleation site (m)
En	enhancement parameter (11)
G	mass velocity (kg/m^2 s)
h_{fg}	latent heat of vaporization (J/kg)
h_{sp}	single-phase heat transfer coefficient (W/m^2 °C)
h_{tp}	two-phase heat transfer coefficient (W/m^2 °C)
I	electrical current (A)
k_l	thermal conductivity of the liquid (water) (W/m °C)
k_s	thermal conductivity of the substrate (silicon) (W/m °C)
L	distance from the inlet of the microchannel (m)
L_0	channel length (m)
p	pressure (kPa)
P	electrical power (W)
q''	heat flux (W/cm^2)
q''_{ch}	channel wall heat flux (6) (W/cm^2)
q''_{eff}	effective heat flux (5) (W/cm^2)
$\dot{Q}_{loss}$	heat loss (W)
R	electrical resistance (ω)
t	thickness of the silicon substrate (m)
T	temperature (°C)
T_{avg}	average surface temperature (°C)
T_f	fluid temperature (°C)
$\bar{T}_{heater}$	average heater temperature (°C)
T_s	local surface temperature (°C)
$T_{thermistor}$	thermistor temperature (°C)
T_w	channel wall temperature (°C)
ΔT_w	wall superheat (°C)
ΔT_{sub}	subcooled temperature (°C)
V	electrical voltage (V)
x	local mass quality

Greek symbols

δ_t	thermal boundary layer thickness (m)
ϕ	contact angle (°)
ρ	density (m^3/s)
σ	surface tension (N/m)

Subscripts

avg	average
ch	channel
eff	effective
f	fluid
l	liquid
max	maximum
min	minimum
sat	saturation
sp	single-phase
sub	subcooled
tp	two-phase
v	vapor

unknown about flow boiling in enhanced surface microchannels. The onset of nucleate boiling, the local heat transfer coefficient, flow morphologies, and the critical heat flux conditions are poorly understood at diminishing length scales, especially in channels with enhanced structures. Furthermore, the relation between flow boiling patterns and the heat transfer mechanism still remain unclear because of lack of local temperature (and two-phase heat transfer coefficient) measurements. The current investigation presents a detailed examination of flow boiling through enhanced 223 μm hydraulic diameter microchannels with reentrant type cavities. The study involves an in-depth evaluation of the fundamental processes comprising the boiling mechanism under a range of thermal and hydrodynamic conditions. Flow boiling patterns, onset of nucleate boiling, heat transfer coefficients, and critical heat fluxes are presented and discussed. Comparisons between enhanced-surface channel and plain-wall channel are also made. The microchannel device overview is presented in Section 2. The experiment procedures and descriptions of the design, fabrication and experimental setup are provided in Section 3. Section 4 is devoted to the discussion of the experimental results and Section 5 presents the conclusions of this investigation.

2. Device overview

A computer aided design (CAD) model of the microchannel device consisting of five parallel 10,000 μm long, 200 μm wide, and 253 μm deep microchannels, spaced 200 μm apart, is shown in Fig. 1. Scanning electron microscope (SEM) images of the microchannels are also shown in Fig. 2. Each sidewall encompasses an array of 100 reentrant cavities spaced 100 μm apart. An acute angle connects the 7.5 μm mouth to the 25 μm inside diameter reentrant body (Fig. 2c). In order to minimize ambient heat losses, an air gap is formed on the two ends of the side walls (Fig. 1), and an inlet and exit plenum are etched on the thin silicon substrate (~150 μm). A 20 μm wide and 400 μm long orifice is installed at the entrance of each channel inlet to suppress flow instabilities. At the top of the device, a Pyrex cover seals the device from the top and allows flow visualization. Fig. 3a depicts a CAD model of the backside of the device. Three thermistors 10 μm wide and 300 μm long (Fig. 3b) are located 3400 μm, 6700 μm, and 10,000 μm downstream the channel inlet together with electrical connecting vias. On top of the thermistors layer, a 1 μm silicon oxide layer is deposited for electrical insulation. A heater is then formed on top of the oxide layer to

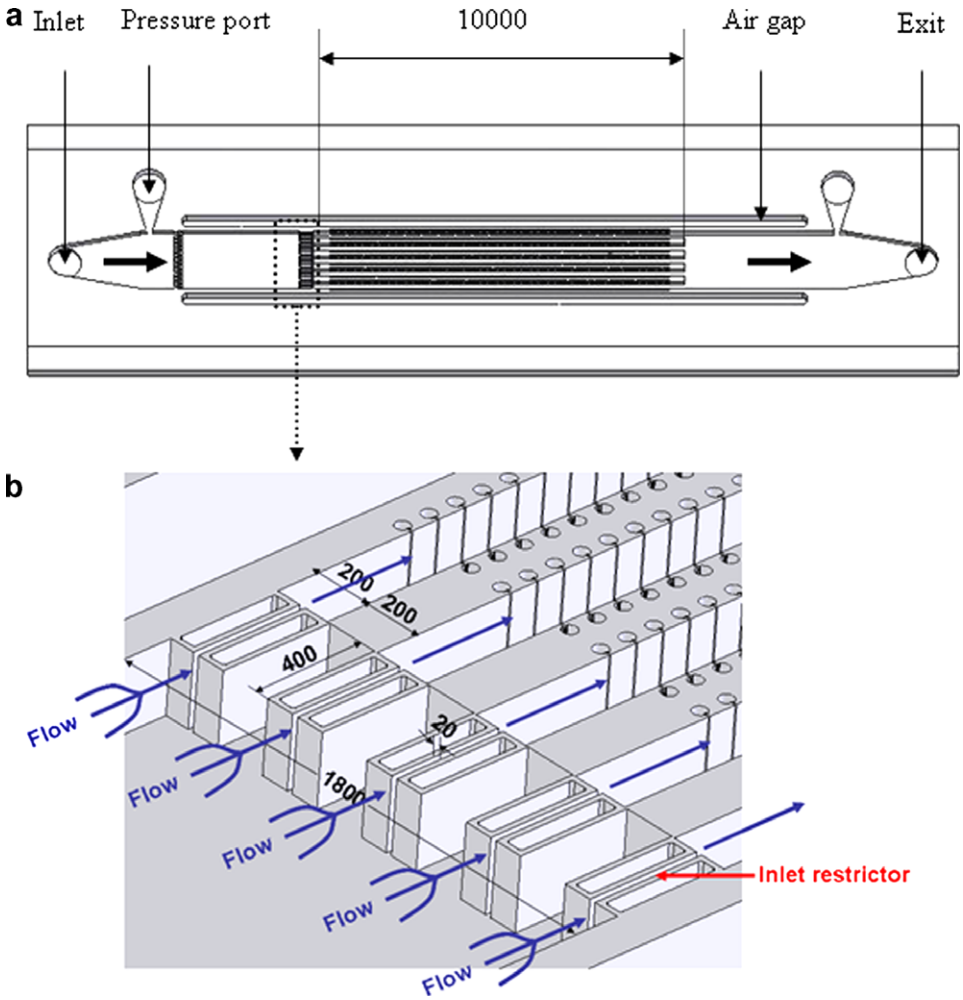

Fig. 1. (a) CAD model of the microchannel device and (b) geometry of the orifice configuration (all units in μm).

deliver the heating power and also serves as a thermistor to measure the average temperature of the entire microchannel area.

3. Device fabrication, experimental apparatus, and procedures

3.1. Microchannel fabrication method

The MEMS device was micromachined on a polished double-sided n-type ⟨100⟩ single crystal silicon wafer employing techniques adapted from integrated circuit (IC) manufacturing. A 1 μm thick high-quality oxide film was deposited on both sides of the silicon wafer to shield the bare wafer surface during processing and to serve as an electrical insulator. A layer of 150 Å thick titanium was deposited by a cyropumped CVC 601 sputter deposition system and patterned on the backside of the wafer to form the thermistors. Vias of 0.2 μm aluminum containing 1% silicon and 4% copper was subsequently formed in order to create electrical connections to the thermistors. Following, a 1 μm thick plasma enhanced chemical vapor deposition (PECVD) oxide was deposited to insulate the thermistors and the vias from the lower layer. The heater was then formed on top of the oxide layer by CVC sputtering deposition. A 70 Å thick layer of titanium was initially deposited to enhance adhesion characteristics and was followed by sputtering a 1 μm thick layer of Al–1%Si–4%Cu. Subsequent photolithography and concomitant wet bench processing created the heater on the backside of the wafer. Another 1 μm thick PECVD oxide was deposited to protect the back side features during further processing.

Next, the microchannels were formed on the top side of the wafer. The wafer was taken through a photolithography step and a reactive ion etching (RIE) oxide removal process to mask certain areas on the wafer, which were not to be etched during the deep reactive ion etching (DRIE) process. The wafer was consequently etched in a DRIE process, and silicon was removed from places not protected by the photoresist/oxide mask. The DRIE process formed deep vertical trenches on the silicon wafer with a characteristic scalloped sidewall possessing a peak-to-peak roughness of ~0.3 μm. A profilometer and SEM were employed to measure and record various dimensions of the device.

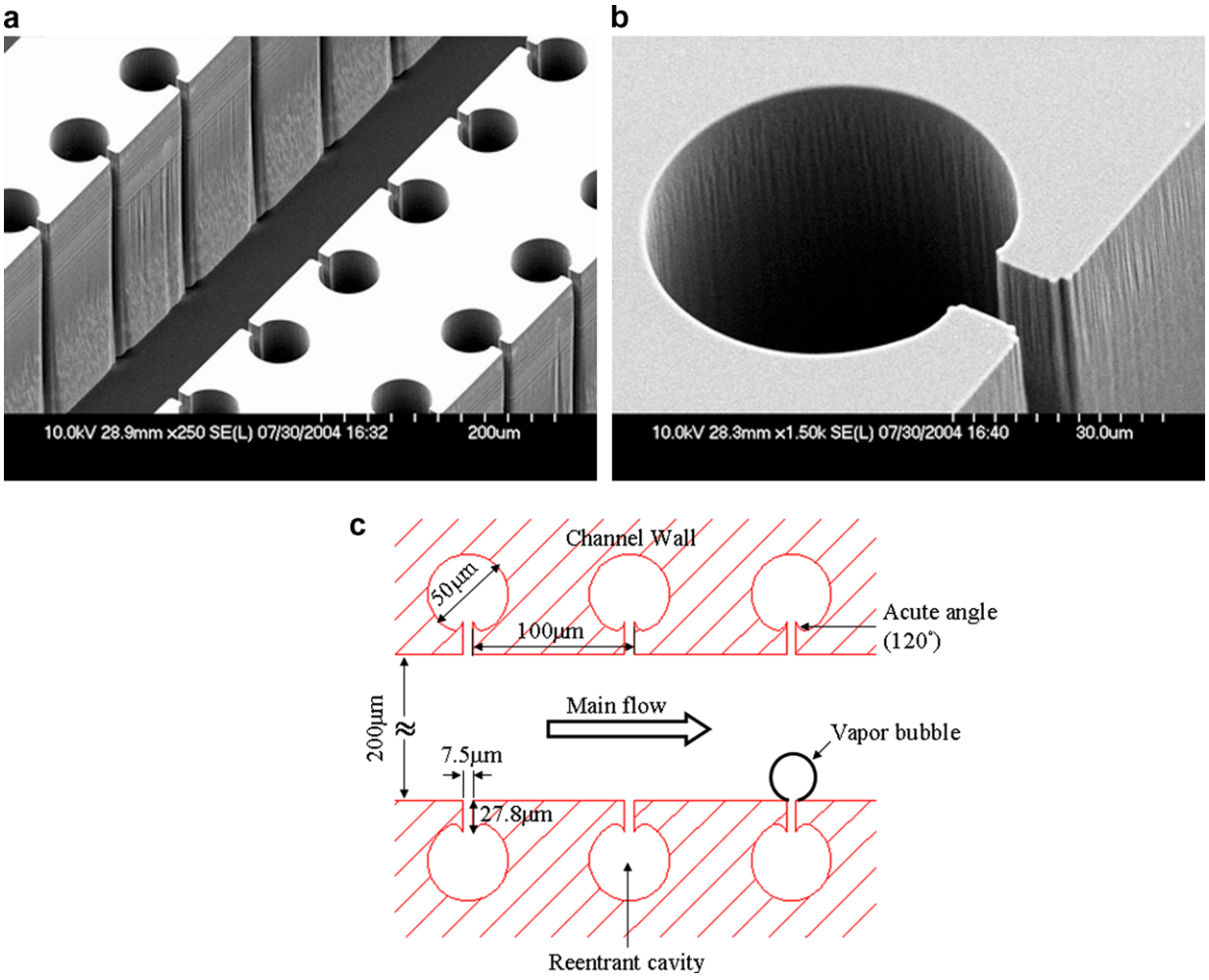

Fig. 2. Reentrant cavities (a,b) SEM images and (c) geometry configuration of reentrant cavities.

The wafer was flipped, and the backside was then processed to create an inlet, outlet, side air gap, and pressure port taps for the transducers. A photolithography step followed by a buffered oxide etch (BOE) (6:1) oxide removal process was carried out to create a pattern mask. The wafer was then etched-through in a DRIE process to create the fluidic ports. Thereafter, electrical contacts/pads were opened on the backside of the wafer by performing another round of photolithography and RIE processing. Finally, the processed wafer was stripped of any remaining resist or oxide layers and anodically bonded to a 1 mm thick polished Pyrex (glass) wafer to form a sealed device. After successful completion of the bonding process, the processed stack was die-sawed to separate the devices from the parent wafer. In order to make comparison between the microchannel with and without the reentrant cavities, devices with plain-wall microchannels were also fabricated on the same parent wafer. As a result, they have similar characteristics as the enhanced-surface device.

The MEMS devices were packaged by sandwiching it between two plates (schematically shown in Fig. 4a). The fluidic seals were forged using miniature "o-rings," while the external electrical connections to the thermistors and the heater were achieved from beneath through spring-loaded pins, which connected the thermistors and the heater to electrical pads residing away from the main microchannel body.

3.2. Experimental test rig

The setup, shown in Fig. 4b, consists of three primary subsystems: the flow loop section, instrumentation, and a data acquisition system. The test section houses the MEMS microchannel devices and its fluidic and thermal packaging module. The microchannel device is mounted on the fluidic packaging module through o-rings to ensure a complete leak-free system. The fluidic packaging delivers the working fluid and access to the pressure transducers. The heater, which is fabricated on the device backside, is wired (through electric pads) to the power supply. The thermistors are also connected to a National Instruments SCXI-1000 series data acquisition system.

The main flow loop includes the microchannel device, a pulseless gear pump, a reservoir, which consists of a

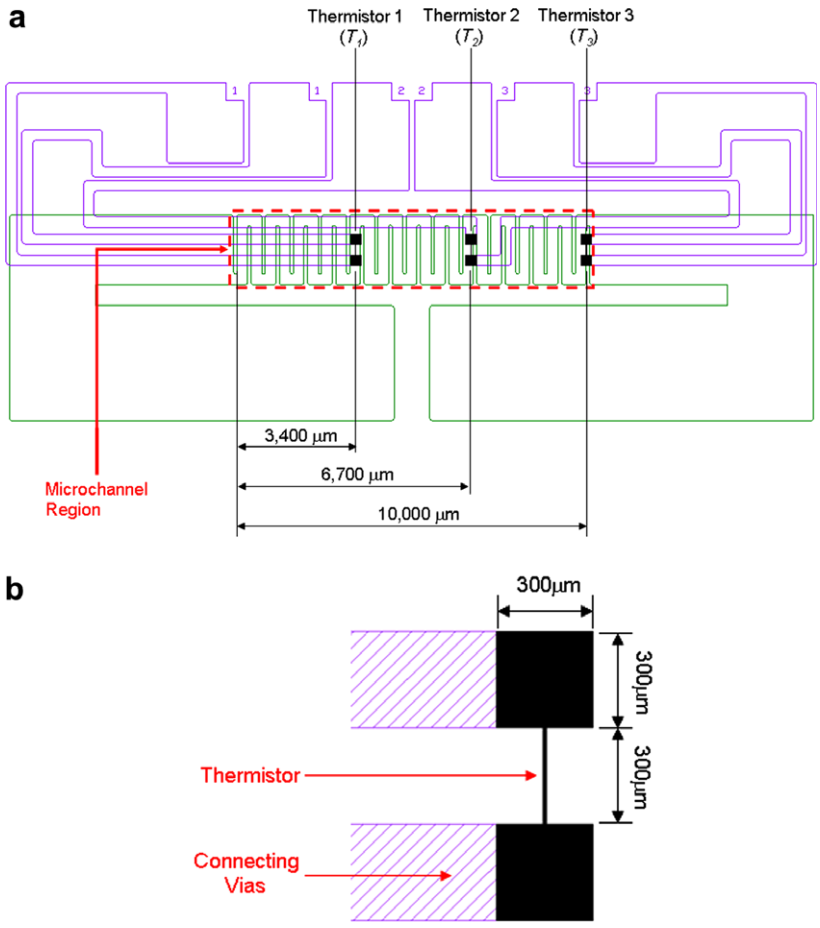

Fig. 3. CAD models of (a) the heater and the thermistors on the back side of the micro-device and (b) a single thermistor.

deaerator unit and a heating element to control the inlet temperature, a flow meter, and a dissolved oxygen meter. The test section heater is connected to a power supply with an adjustable DC current to provide power to the device. The thermistors output signals are recorded by the data acquisition system. Simultaneously, the inlet pressure and test section pressure drop are collected, and the boiling process in the microchannels is recorded by a Phantom V4.2 high-speed camera (maximum frame rate of 90,000 frames/s, and 2 μs exposure time) mounted over a Leica DMLM microscope. Calibration of the heater and the thermistors is performed prior to the experiment by placing the device in an oven and establishing the resistance–temperature curve for each individual sensor.

3.3. Experimental procedures and data reduction

The deionized water was first degassed until the oxygen concentration level dropped below 3 ppm. Then, the water flow rate was fixed at the desired value, and experiments were conducted after steady hydraulic conditions were reached with an exit atmospheric pressure and ambient room temperature (~22 °C). The electrical resistances of the thermistors were also measured at room temperature. During the experiment, voltage was applied in 0.5 V increments to the test section heater, and the resistance data for the heater and the thermistors were recorded once steady thermal–hydraulic state was reached, at which water flow rate, heat input, and resistance data remained constant. The procedure was repeated for different flow rates.

To estimate heat losses, electrical power was applied to the test section after evacuating the water from the test loop. Once the temperature of the test section became steady, the temperature difference between the ambient and test section was recorded with the corresponding power. The plot of power versus temperature difference was used to calculate the heat loss ($\dot{Q}_{\text{loss}}$) associated with each experimental data point.

Data obtained from the voltage, current, and pressure measurements were used to calculate the average single- and two-phase temperatures, the heat transfer coefficients, and the CHF conditions. The electrical input power, P, and heater resistance, R, respectively, were determined by the measured voltage, V, and current, I, with

$$P = V \times I \tag{1}$$

and

$$R = V/I \tag{2}$$

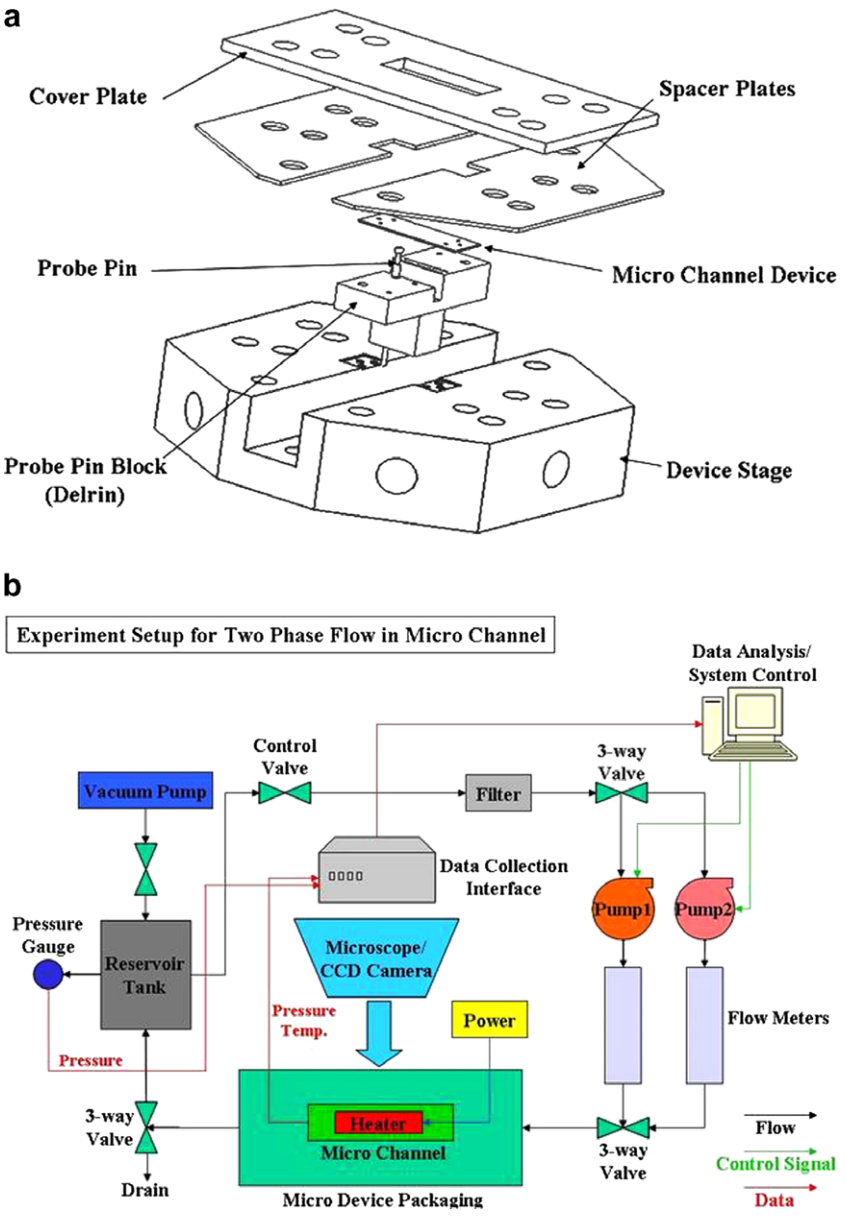

Fig. 4. (a) Device package and (b) experiment setup.

The electrical resistance–temperature calibration curve of the heater and the thermistors were used for determining the average heater temperature, $\bar{T}_{\text{heater}}$, and the thermistor temperature for each local position, $T_{\text{thermistor}}$. The average surface temperature, T_{avg}, and the local surface temperature, T_{s}, at the base of the microchannels was then calculated as

$$T_{\text{avg}} = \bar{T}_{\text{heater}} - \frac{(P - \dot{Q}_{\text{loss}})t}{k_{\text{s}}A_{\text{p}}} \tag{3}$$

$$T_{\text{s}} = T_{\text{thermistor}} - \frac{(P - \dot{Q}_{\text{loss}})t}{k_{\text{s}}A_{\text{p}}} \tag{4}$$

where t, k_{s}, and A_{p}, are the substrate thickness, thermal conductivity of silicon, and the platform area, respectively.

The effective heat flux, q''_{eff}, and the channel wall heat flux, q''_{ch}, can be defined as

$$q''_{\text{eff}} = \frac{P - \dot{Q}_{\text{loss}}}{A_{\text{p}}} \tag{5}$$

$$q''_{\text{ch}} = \frac{P - \dot{Q}_{\text{loss}}}{A_{\text{t}}} \tag{6}$$

where A_{t} is the total channel surface area. The local mass quality at a distance L from the inlet can be obtained by

$$x = \frac{(P - \dot{Q}_{\text{loss}})(L/L_0) - GA_{\text{s}}C_{\text{p}}(T_{\text{sat}} - T_{\text{in}})}{GA_{\text{s}}h_{\text{fg}}} \tag{7}$$

where L_0, G, and A_{s} are the total channel length, mass velocity, and the total channel cross section area, respec-

tively. With the local surface temperature, T_s, the local two-phase heat transfer coefficient, h_{tp}, can be obtained

$$h_{tp} = \frac{q''_{ch}}{T_s - T_{sat}} \tag{8}$$

3.4. Uncertainty analysis

The uncertainties of the measured values are obtained from the manufacturers' specification sheets, while the uncertainties of the derived parameters are calculated using the method developed by Kline and McClintock [31]. Uncertainty in the mass flux (G), heat flux (q''), temperature (T), mass quality (x), and two-phase convective heat transfer coefficient (h_{tp}) are estimated to be ±1%, ±1%, ±1%, ±3%, and ±9%, respectively.

4. Results and discussion

4.1. Flow morphology

Four prime flow patterns were visualized (depending on the thermal–hydraulic conditions) in the reentrant cavity microchannels prior to the critical heat flux conditions: single-phase, bubbly, slug, and annular flow patterns, as shown in Fig. 5. The extent of the bubbly flow pattern was shown to be dependent on the mass velocity and heat flux. Although at low mass velocity ($G = 83$ kg/m^2 s)

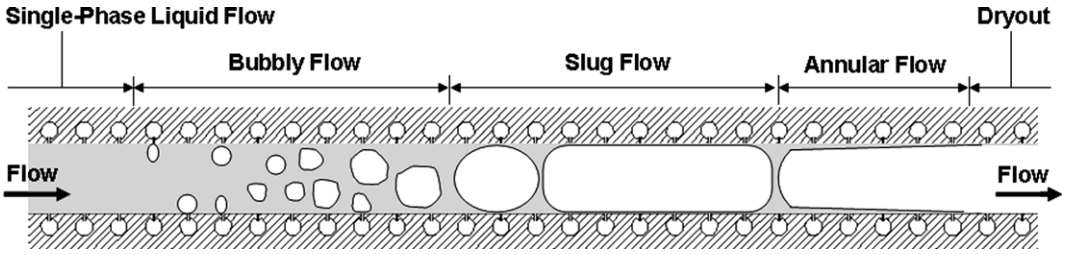

Fig. 5. A schematic representation of the flow patterns.

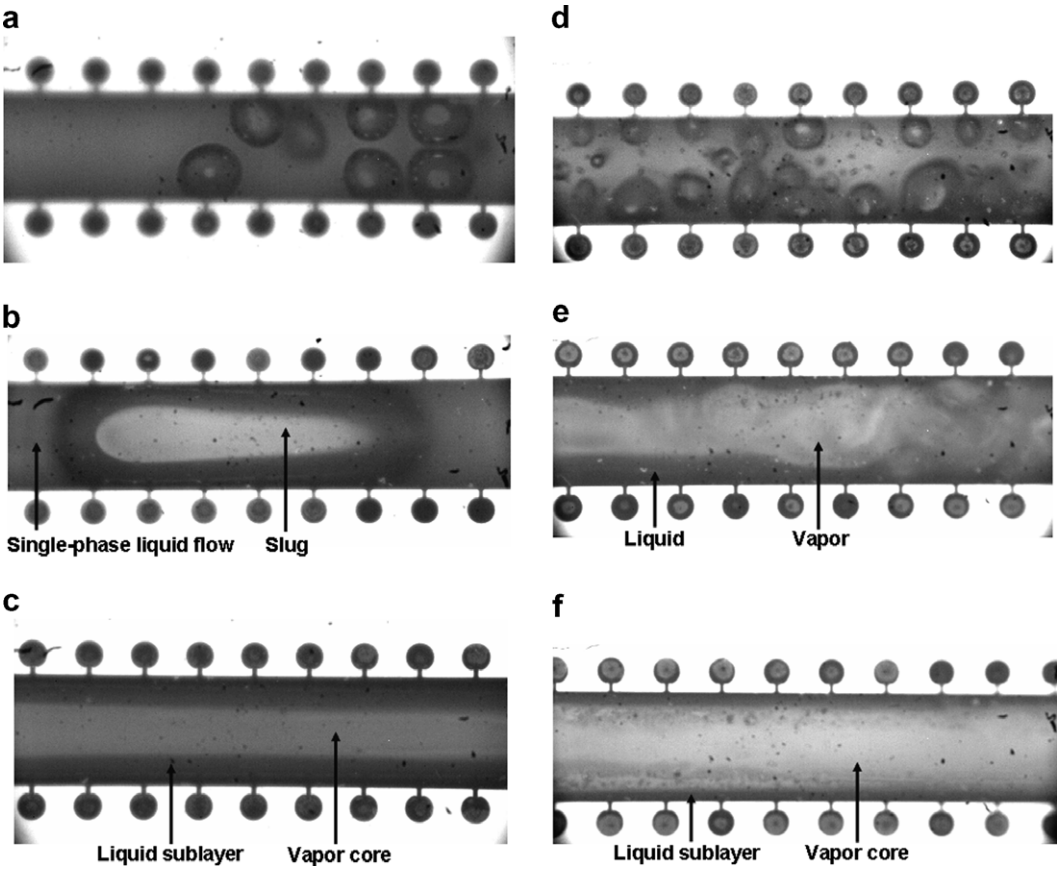

Fig. 6. Flow morphologies: (a) bubbly flow for $G = 83$ kg/m^2 s and $q''_{eff} = 30.6$ W/cm^2; (b) bubbly and slug flow for $G = 83$ kg/m^2 s and $q''_{eff} = 53.2$ W/cm^2; (c) annular flow for $G = 83$ kg/m^2 s and $q''_{eff} = 77.1$ W/cm^2; (d) bubbly flow for $G = 303$ kg/m^2 s and $q''_{eff} = 132.6$ W/cm^2; (e) annular/wavy flow for $G = 303$ kg/m^2 s and $q''_{eff} = 241.6$ W/cm^2; and (f) annular flow for $G = 303$ kg/m^2 s and $q''_{eff} = 585.5$ W/cm^2.

bubbly flow was detected (Fig. 6a), it did not tend to persist over a significant region of the channel, and at sufficient high heat flux, a direct transition from single-phase to slug flow was observed (Fig. 6b). The slug flow was characterized by a large vapor core that occupied the entire microchannel cross section and oscillated rapidly over several hydraulic diameters. Downstream a more stable annular flow was developed (Fig. 6c), which was characterized by a vapor core engulfed by a continuous liquid sublayer attached to the microchannel walls. For higher mass velocities ($G = 303$ kg/m^2 s), reduction in the bubble departure diameter followed by increasing bubble generation frequency was observed (Fig. 6d), which supported bubbly flow over extended channel length. As the bubbles grew and emerged, they formed slugs stretching over several hydraulic diameters. Following the slug flow, an annular–wavy flow was occasionally detected in which the liquid sublayer thickness was unsteady, as shown in Fig. 6e, this was followed by a more stable annular flow. As the mass quality increased, the liquid layer diminished (Fig. 6f) until dry spots at the exit region were detected indicating the arrival of the critical heat flux conditions.

4.2. Boiling curve

Fig. 7 shows T_{avg} and T_2 as functions of the effective heat flux (q''_{eff}) for four different mass velocities. As expected, at low heat fluxes, single-phase liquid flow prevails, which is depicted by the linear temperature increase with increasing surface heat flux. When the heat flux is further increased, a significant shift in the T–q''_{eff} slope is apparent marking the onset of nucleate boiling. Flow visualization reveals small bubbles emerging from the reentrant cavities near the channel exit. A small surface superheat is required for boiling to be established upstream from the exit region, as can clearly be seen in Fig. 7b. As expected,

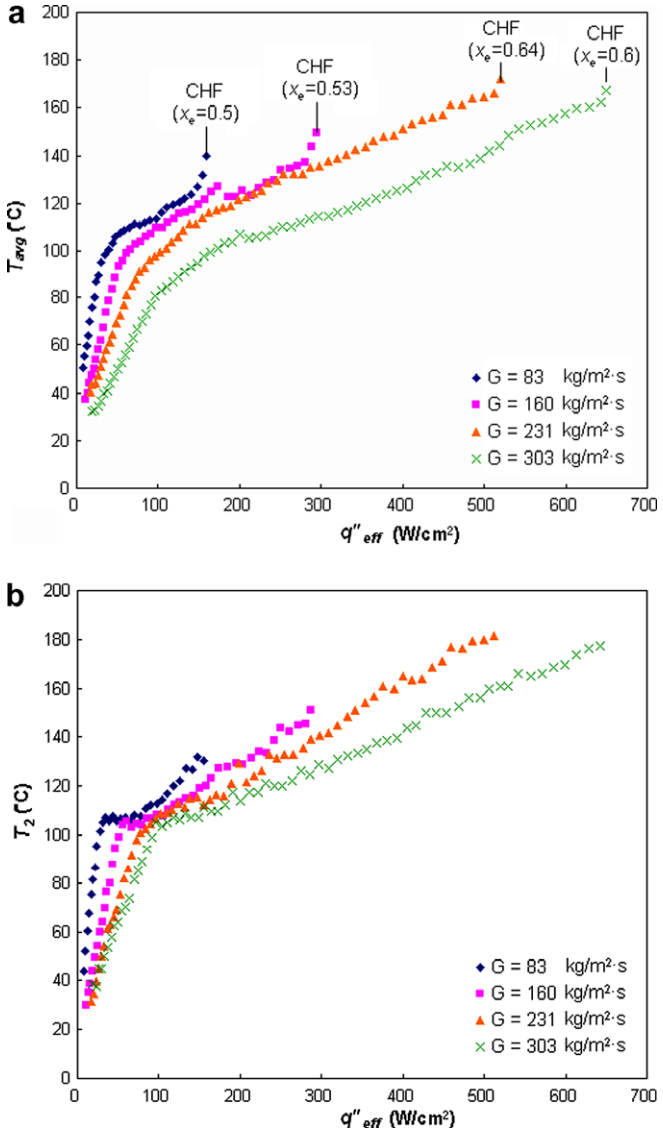

Fig. 7. Temperature as a function of effective heat flux: (a) T_{avg}–q''_{eff} and (b) T_2–q''_{eff}.

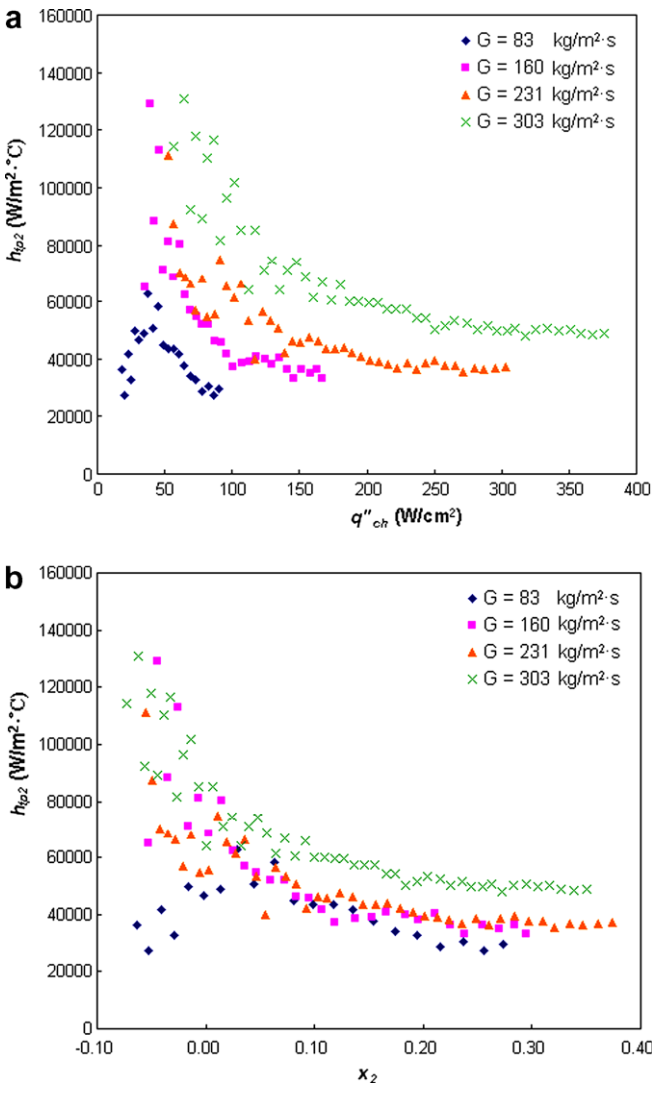

Fig. 8. Two-phase heat transfer coefficient as a function of (a) channel wall heat flux and (b) mass quality.

the transition in the temperature slope from single-phase to flow boiling is much more abrupt in the T_2–q''_{eff} plot than in the T_{avg}–q''_{eff} plot. As the heat flux was further increased above a certain value, the average surface temperature abruptly surged with a meager rise of heat flux, indicating the emergence of critical heat flux condition. The CHF was verified by flow visualizations of dry spots at the channel exit region. Once CHF condition was detected, the power was turned off to prevent damage.

4.3. Two-phase heat transfer coefficient

The local two-phase heat transfer coefficient, h_{tp2}, is shown in Fig. 8 as functions of the channel wall heat flux, q''_{ch}, and mass quality, x. Negative mass quality at the beginning of the boiling process indicates subcooled boiling. Except for a sharp increase at low qualities, the local two-phase heat transfer coefficient for all mass velocities drops and asymptotically reaches a constant value after $x \sim 0.05$

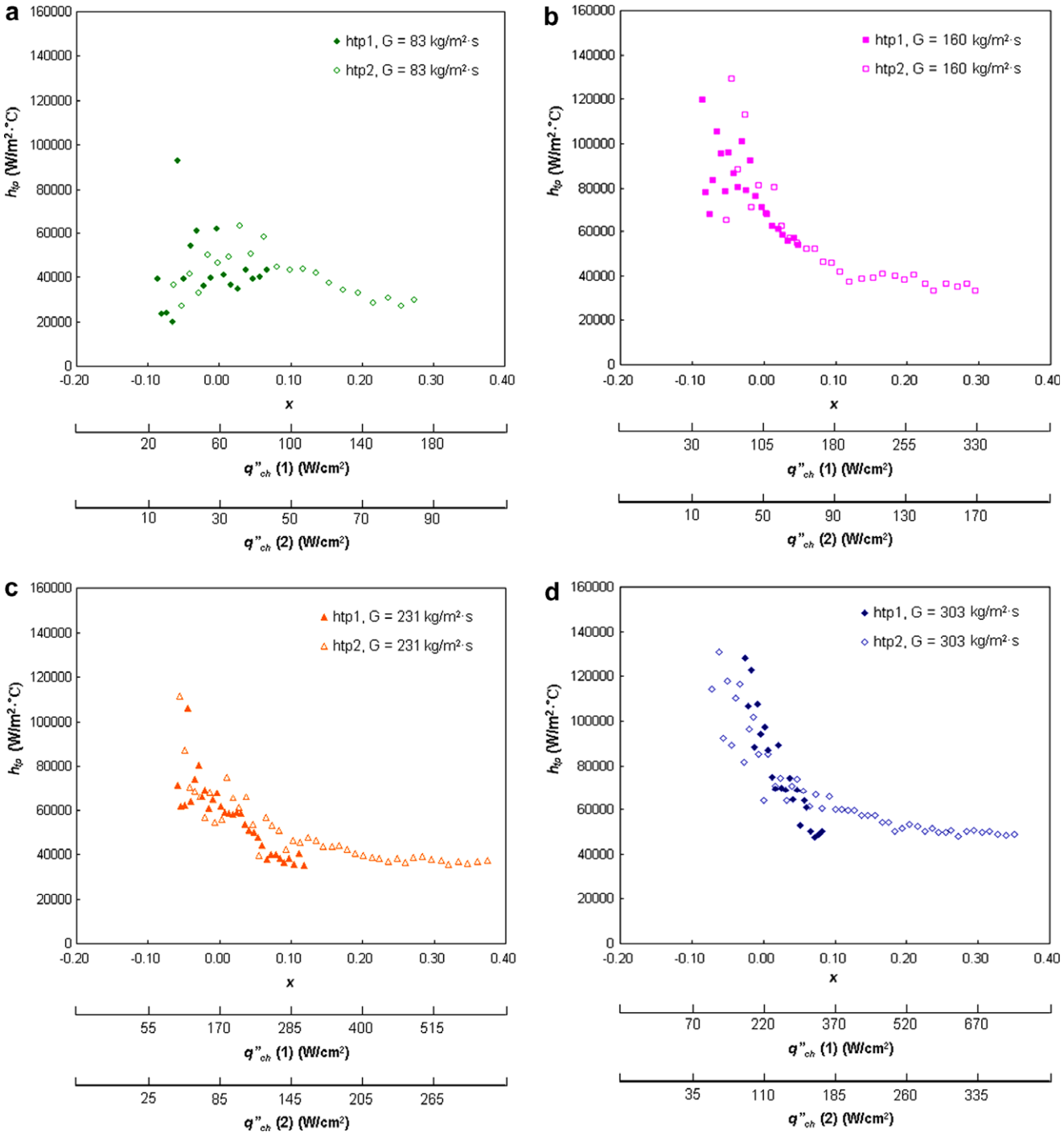

Fig. 9. Comparisons of two-phase heat transfer coefficient at different locations of the channel for (a) $G = 83$ kg/m^2 s, (b) $G = 160$ kg/m^2 s, (c) $G = 231$ kg/m^2 s, and (d) $G = 303$ kg/m^2 s.

until the CHF. It can also be seen from Fig. 8b that h_{tp2} for all mass velocities except for $G = 303$ kg/m^2 s shows nearly no dependence on the mass velocity. Starting at $x \sim 0.05$, h_{tp2} for $G = 303$ kg/m^2 s is significantly higher than for all other mass velocities. Superimposing the two-phase heat transfer coefficient obtained by thermistor 1, h_{tp1}, and thermistor 2, h_{tp2}, (Fig. 9) shows good agreement. It should be noted that for a fixed mass quality, the data for h_{tp1} and h_{tp2} in Fig. 9 correspond to considerably different heat flux, which are also illustrated as q''_{ch} (1) and q''_{ch} (2) on the figure. Thus, it can be inferred that the heat transfer coefficient is not a strong function of the heat flux, at least at low qualities. The independence of the mass velocity and quality for $G \leqslant 231$ kg/m^2 s suggests that convective boiling might not be the dominant heat transfer mechanism at low to moderate mass velocities. For high mass velocity convective boiling heat transfer mechanism cannot be ruled out. However, as discussed earlier, flow visualization clearly reveals (Fig. 6d) myriad bubbles growing and departing from numerous reentrant cavities at high mass velocities, implying that convective boiling is not the only mechanism controlling the heat transfer process. Some complications in identifying the dominant heat transfer mechanism arise from the weak dependency of the two-phase heat transfer coefficient on the heat flux, as implied by Fig. 9. In conventional scale systems with boiling-enhanced surface, nucleate boiling heat transfer is linked with significant dependency of the heat transfer coefficient on the heat flux [9–13]. Thus, the results suggest that the heat transfer process in the current system may be more convoluted than similar systems at conventional scale.

4.4. Comparison with plain-wall microchannel

To evaluate the heat transfer enhancement performance of the reentrant cavity microchannel, ONB, local heat transfer coefficient, and CHF were also obtained for a plain-wall microchannel at similar thermal–hydraulic conditions. Comparisons of the heat flux at ONB at different mass velocities in the enhanced and plain microchannels are given in Fig. 10. As can clearly be seen, the onset of nucleate boiling commences at significantly lower heat fluxes for the boiling-enhanced surface microchannel compared to the plain-wall channel. The effective heat flux for the ONB condition is ~70% higher in the plain-wall channel than in the enhanced-surface channel for all mass velocities. These results clearly show that the reentrant cavities are very effective in triggering boiling at much lower superheated surface temperature than plain channels. Hsu's model [32] provides the size of active nucleation site, D_c, and is given by the following equation:

$$\{D_{c,max}, D_{c,min}\} = \frac{\delta_t C_2}{2C_1} \frac{\Delta T_w}{\Delta T_w + \Delta T_{sub}} \times \left[1 \pm \sqrt{1 - \frac{8C_1 \sigma T_{sat}(p_l)(\Delta T_w + \Delta T_{sub})}{\rho_v h_{fg} \delta_t (\Delta T_w)^2}}\right] \quad (9)$$

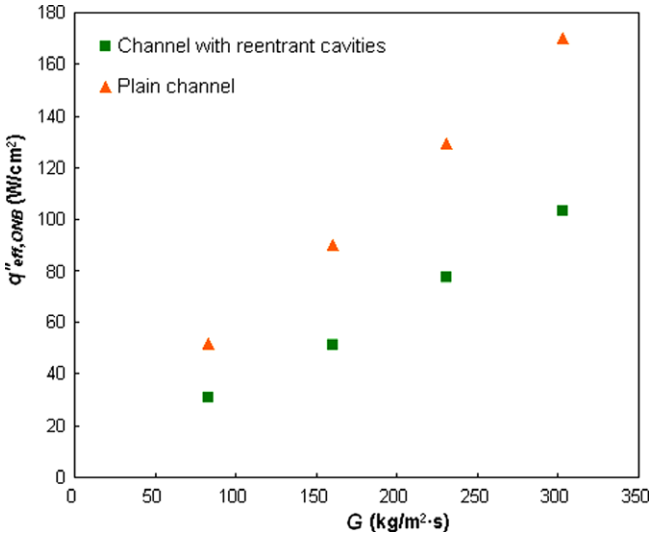

Fig. 10. Comparison of effective heat flux at ONB for the channel with reentrant cavities and the plain-wall channel.

where $C_1 = 1 + \cos\phi$, $C_2 = \sin\phi$, $\Delta T_w = T_w - T_{sat}$, $\Delta T_{sub} = T_{sat} - T_f$, σ, δ_t, and ϕ are surface tension, thermal boundary layer thickness, and contact angle, respectively. Assuming linear temperature profile in the liquid boundary layer, as is commonly postulated in similar large scale systems [33], the thermal boundary layer thickness δ_t can be simply expressed as

$$\delta_t = \frac{k_l}{h_{sp}} \quad (10)$$

For $Nu = 5.5$ (thermal and hydraulic fully developed flow), $\delta_t \sim 40$ μm. For contact angle $\phi = 57°$, nucleation sites with mouth diameter 12 μm $\geqslant D_c \geqslant$ 4 μm are most effective in reducing the surface superheat required for the onset of nucleate boiling in the current microchannel, as shown in Fig. 11. Clearly surface roughness of 0.3 μm (typical of

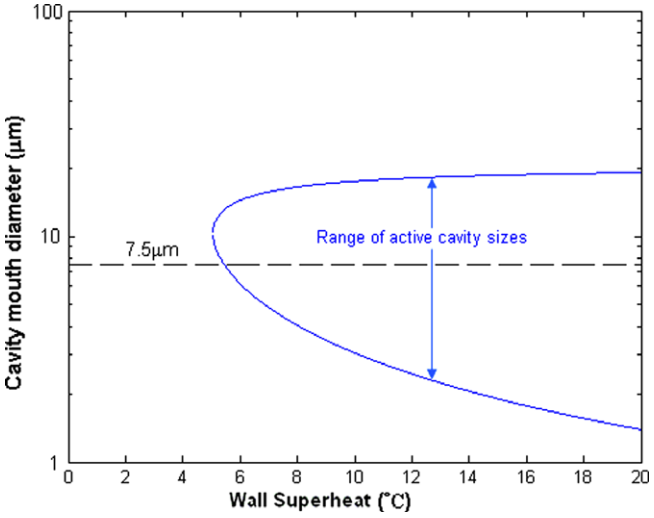

Fig. 11. Range of active cavity size as a function of wall superheat for the current microchannel based on Hsu's criteria.

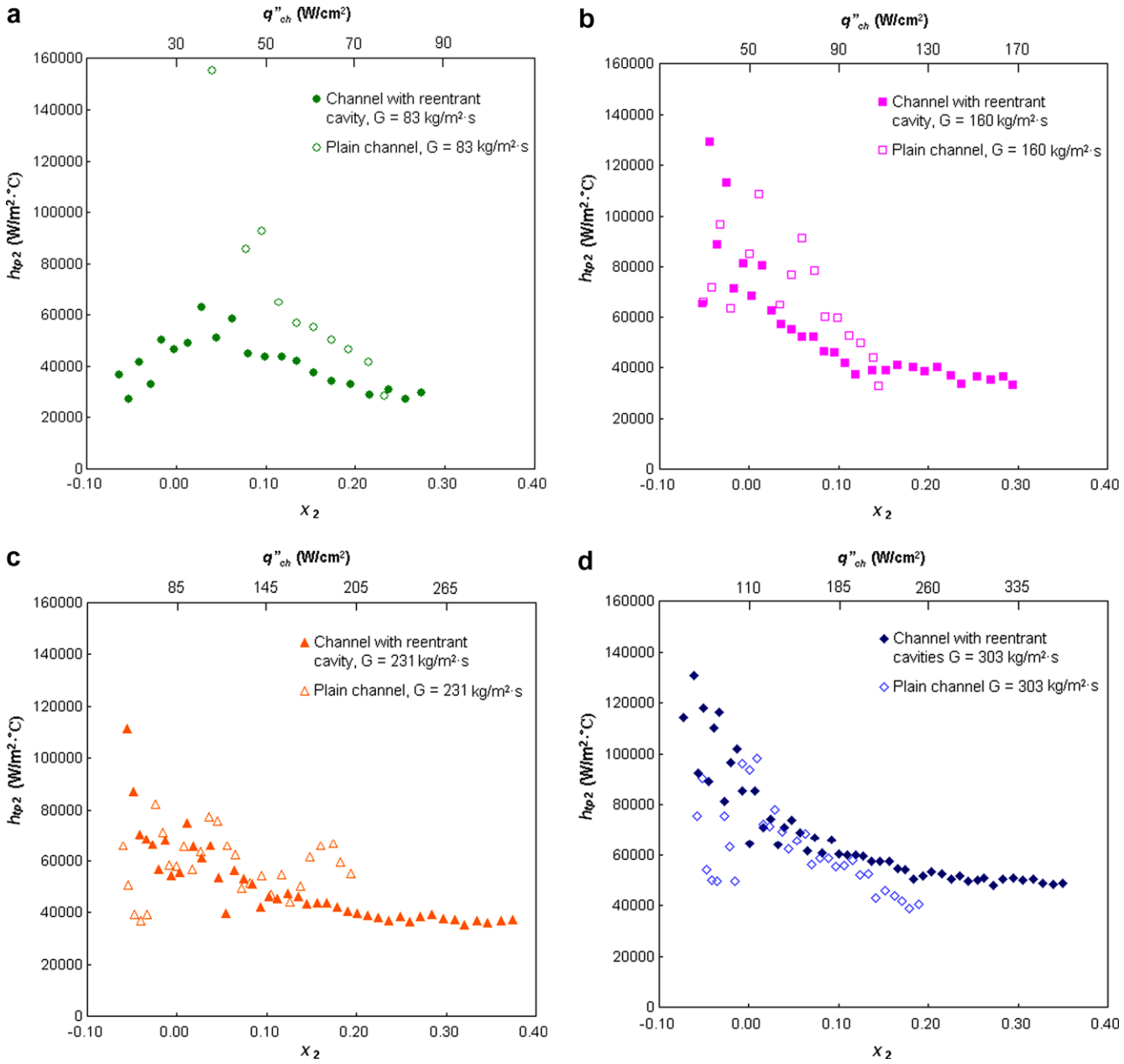

Fig. 12. Comparisons of the two-phase heat transfer coefficient for the microchannel with reentrant cavities and the plain channel for (a) $G = 83$ kg/m^2 s, (b) $G = 160$ kg/m^2 s, (c) $G = 231$ kg/m^2 s, and (d) $G = 303$ kg/m^2 s.

plain-wall microchannel) will result in much higher surface temperature, as indeed evident from Fig. 10.

Fig. 12 compares the local two-phase heat transfer coefficient, h_{tp2}, as a function of quality, x_2, and channel wall heat flux, q''_{ch}, for the enhanced-surface and the plain-wall channels. Similar to the enhanced-surface, for all mass velocities, h_{tp2} in the plain-wall channel does not seem to have significant dependence on the quality or mass velocity. Furthermore, it can be seen that h_{tp2} is greater in the enhanced-surface channel than in the plain-wall channel for $G = 303$ kg/m^2 s, but smaller for $G = 83$ kg/m^2 s and $G = 160$ kg/m^2 s. To provide a quantitative measurement of the deviation of the two-phase heat transfer coefficient between the enhanced-surface and the plain-wall channel, a new parameter, En, is introduced and defined as following:

$$\mathrm{En} = \frac{h_{tp} \text{ in enhanced-surface channel}}{h_{tp} \text{ in plain-wall channel}} \tag{11}$$

En as a function of quality for different mass velocities is shown in Fig. 13. The significant enhancement of the two-phase heat transfer coefficient at high mass velocity (~30%) can be linked to the considerable increase in the nucleation site density and bubble departure frequency with increasing mass velocities. For low mass velocity, the deviation of the flow patterns (which is linked to the

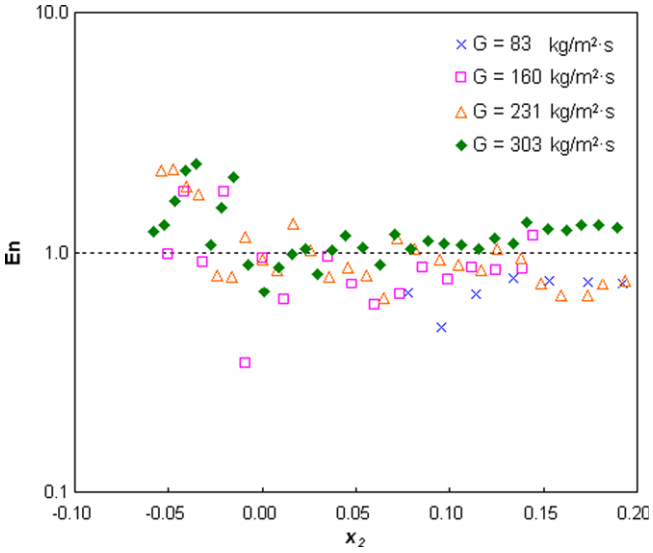

Fig. 13. En as a function of quality for four different mass velocities.

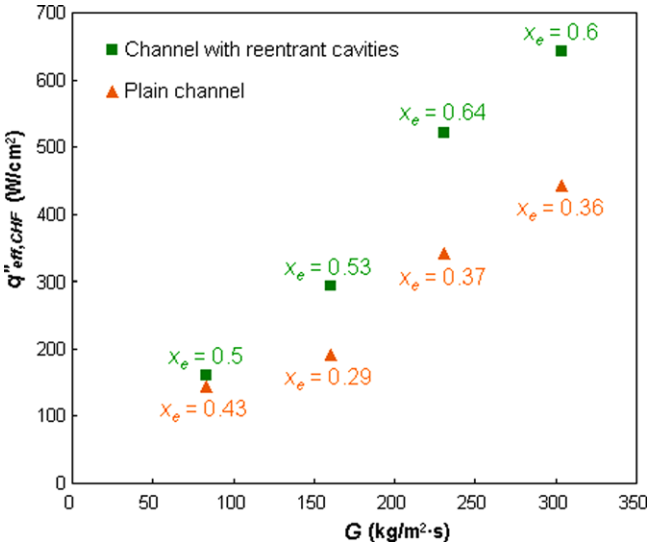

Fig. 14. Comparison of the critical heat flux for the channel with reentrant cavities and the plain-wall channel. The corresponding exit qualities are also indicated.

heat transfer mechanism) between the enhanced-surface and plain-wall channel is less apparent than for high mass velocity. The moderately lower heat transfer coefficient of the enhanced-surface channel at low mass velocities is perhaps a result of somewhat lower fin efficiency of the enhanced channel wall.

Another important aspect of flow boiling in parallel channels is the flow and heat transfer uniformity between channels. For microchannels with reentrant cavities, deviation in the boiling length between the channels is small with continuous upstream supply of bubbles. On the other hand, significant non-uniformity in the boiling length for the plain channel is observed. It can be concluded that the reentrant cavities channels are also very effective in maintaining consistent and repeatable flow boiling conditions. The increased uniformity is a result of the availability of effective nucleation sites that can be easily activated at low superheat temperature. On the other hand, the high superheat required to activate nucleation sites in the plain channel (with average mouth diameter ~0.3 μm) tends to form a more random and non-uniform nucleation process. The limited nucleation activity promotes flow oscillations, which in term can trigger premature critical heat flux conditions, as discussed in the next section.

4.5. Critical heat flux

Fig. 14 compares the critical heat flux at different mass velocities in the enhanced-surface and plain-wall microchannels (the exit quality is also indicated). The CHF of the enhanced surface is much larger than for the plain-wall channel, with an increase of 11%, 55%, 52%, and 45% for $G = 83$ kg/m^2 s, $G = 160$ kg/m^2 s, $G = 231$ kg/m^2 s, and $G = 303$ kg/m^2 s, respectively. The increase in the CHF value for the reentrant cavities microchannel may be linked to the increased uniformity and reproducibility of the boiling process in the enhanced channel. The establishment of a more orderly boiling process with more uniform and smaller bubbles tends to suppress flow oscillations and instabilities. In systems with significant deficit of nucleation sites (e.g., plain-wall microchannels), the boiling process commences at high liquid superheats. Under such conditions the liquid–vapor phase-change process tends to be exceedingly rapid, instigating hydrodynamic oscillations. It has been argued by various researchers [34–37] that flow oscillations are closely connected to premature CHF conditions. Although inlet restrictors, similar to the ones used in the current study, had been shown to be very effective in suppressing parallel channel and upstream compressible flow instabilities [37], some compressible volume within the microchannel exists. It has been shown that the upstream compressibility required for unstable behavior is small, and small volumes of cold water can produce a large reduction in the CHF, especially for small diameter tubes [38].

5. Conclusion

Experiments were conducted to investigate flow boiling heat transfer in microchannels with reentrant cavities. Flow morphologies, boiling inceptions, heat transfer coefficients, and the critical heat fluxes have been obtained and studied. Comparisons of the performance of the enhanced and plain-wall microchannels were also performed. The main conclusions drawn from this study are presented below:

(1) Intensified nucleation activity was observed in the microchannels with reentrant cavities with significantly better uniformity of nucleation site distribution.
(2) Flow patterns in microchannels with reentrant cavities are similar to those in conventional scale channel.

Bubbly flow was minimal to non-existent for low mass velocity. For high mass velocity, vigorous bubble nucleation activity together with an extended bubbly region was observed.

(3) For low mass velocities ($G \leqslant 231$ kg/m^2 s), nucleate boiling was shown to be dominated for flow boiling in enhanced microchannel. For higher mass velocity, the heat transfer mechanism was shown to be more convoluted.

(4) Significant reductions in the wall superheat required to initiate boiling were measured with the enhanced-surface microchannel compared to the plain-wall microchannel. The result is consistent with the theoretical prediction of the effective nucleation size.

(5) The bubble nucleation process in the structured surface microchannel is much more consistent and reproducible than in the plain channel. Combined with the increased nucleation activity, this enhanced consistency and reproducibility suppressed flow oscillations and assisted in the enhancement of the critical heat flux in the reentrant cavity microchannel.

Acknowledgement

This work was supported by the Office of Naval Research through the Young Investigator Program under Contact No. N00014-05-1-0582.

References

[1] J.R. Thome, Enhanced Boiling Heat Transfer, Hemisphere, 1990.
[2] R.L. Webb, The evolution of enhanced surface geometries for nucleate boiling, Heat Transfer Eng. 2 (3–4) (1981) 46–69.
[3] P. Griffith, J.D. Wallis, The role of surface conditions in nucleate boiling, Chem. Eng. Prog. Symp. 56 (49) (1960) 49–63.
[4] R.F. Gaertner, J.W. Westwater, Population of active sites in nucleate boiling heat transfer, Chem. Eng. Prog. Symp. 56 (1960) 39–48.
[5] B. Mikic, W.M. Rohsenow, A new correlation of pool boiling data including the effect of heating surface characteristic, J. Heat Transfer 91 (1969) 245–250.
[6] K. Cornwell, R.D. Brown, Boiling surface topography. in: Proceeding of the Sixth International Heat Transfer Conference, Toronto, vol. 1, 1978, pp. 157–161.
[7] K. Bier, D. Gorenflo, M. Salem, Y. Tanes, Pool boiling heat transfer and size of active nucleation centers for horizontal plates with different surface roughness. in: Proceeding of the Sixth International Heat Transfer Conference, Toronto, vol. 1, 1978, pp. 151–156.
[8] L.Z. Zeng, J.F. Klausner, Nucleation site density in forced convection boiling, J. Heat Transfer 115 (1993) 215–221.
[9] R.L. Webb, Nucleate boiling on porous coated surfaces, Heat Transfer Eng. 4 (3–4) (1983) 71–82.
[10] C.F. Gottzmann, P.S. O'Neill, P.E. Minton, High efficiency heat exchangers, Chem. Eng. Prog. 69 (7) (1973) 69–75.
[11] R. Roser, B. Thonon, P. Mercier, Experimental investigations on boiling of *n*-pentane across a horizontal tube bundle: two-phase flow and heat transfer characteristics, Int. J. Refrig. 22 (1999) 536–547.
[12] J.Y. Chang, S.M. You, Boiling heat transfer phenomena from microporous surfaces in saturated FC-72, Int. J. Heat Mass Transfer 40 (18) (1997) 4437–4447.
[13] J.Y. Chang, S.M. You, Enhanced boiling heat transfer from microporous surfaces: effect of coating composition and method, Int. J. Heat Mass Transfer 40 (18) (1960) 4447–4449.
[14] W. Nakayama, T. Nakajima, S. Hirasawa, Heat sink studs having enhanced boiling surfaces for cooling microelectronic components, ASME Paper No. 84-WA/HT-89, 1984.
[15] L.H. Chien, R.L. Webb, A nucleate boiling model for structured enhanced surfaces, Int. J. Heat Mass Transfer 41 (1998) 2183–2195.
[16] S. Murthy, Y. Joshi, S. Gurrum, W. Nakayama, Enhanced boiling heat transfer simulation from structured surfaces: semi-analytical model, Int. J. Heat Mass Transfer 49 (2006) 1885–1895.
[17] L. Zhang, J. Koo, L. Jiang, M. Asheghi, K.E. Goodson, J.G. Santiago, Measurements and modeling of two-phase flow in microchannels with nearly constant heat flux boundary conditions, IEEE JMEMS 11 (1) (2002) 12–19.
[18] L. Jiang, M. Wong, Y. Zohar, Forced convection boiling in microchannel heat sink, IEEE JMEMS 10 (1) (2001) 80–87.
[19] S.G. Kandlikar, Fundamental issues related to flow boiling in minichannels and microchannels, Exp. Therm. Fluid Sci. 26 (2002) 389–407.
[20] W. Qu, I. Mudawar, Flow boiling heat transfer in two-phase microchannel heat sinks—I. Experimental investigation and assessment of correlation methods, Int. J. Heat Mass Transfer 46 (2003) 2755–2771.
[21] W. Qu, I. Mudawar, Flow boiling heat transfer in two-phase microchannel heat sinks—II. Annular two-phase flow model, Int. J. Heat Mass Transfer 46 (2003) 2773–2784.
[22] H. Honda, J.J. Wei, Enhanced boiling heat transfer from electronic components by use of surface microstructures, Exp. Therm. Fluid Sci. 28 (2–3) (2004) 159–169.
[23] H. Honda, H. Takamatsu, J.J. Wei, Enhanced boiling heat transfer from silicon chips with micro-pin fins immersed in FC-72, J. Enhanc. Heat Transfer 10 (2) (2003) 211–223.
[24] J.J. Wei, H. Honda, Effects of fin geometry on boiling heat transfer from silicon chips with micro-pin-fins immersed in FC-72, Int. J. Heat Mass Transfer 46 (21) (2003) 4059–4070.
[25] H. Honda, H. Takamastu, J.J. Wei, Enhanced boiling of FC-72 on silicon chips with micro-pin-fins and submicron-scale roughness, J. Heat Transfer 124 (2) (2002) 383–390.
[26] L. Zhang, E.N. Wang, K.E. Goodson, T.W. Kenny, Phase change phenomena in silicon microchannels, Int. J. Heat Mass Transfer 48 (8) (2005) 1572–1582.
[27] A. Koşar, C.-J. Kuo, Y. Peles, Boiling heat transfer in rectangular microchannels with reentrant cavities, Int. J. Heat Mass Transfer 48 (23–24) (2005) 4867–4886.
[28] A. Koşar, C.-J. Kuo, Y. Peles, Reduced pressure boiling heat transfer in rectangular microchannels with interconnected reentrant cavities, J. Heat Transfer 127 (10) (2005) 1106–1114.
[29] C.-J. Kuo, A. Koşar, Y. Peles, S. Virost, C. Mishra, M.K. Jensen, Bubble dynamics during boiling in enhanced surface microchannels, IEEE JMEMS 15 (6) (2005) 1514–1527.
[30] D.T. Pate, R.J. Jones, S.H. Bhavnani, Cavity-induced two-phase heat transfer in silicon microchannels, in: Thermomechanical Phenomena in Electronic Systems – Proceedings of the Intersociety Conference, v 2006, 10th Intersociety Conference on Thermal and Thermomechanical Phenomena and Emerging Technologies in Electronic Systems, ITherm, 2006, pp. 71–78.
[31] S. Kline, F.A. McClintock, Describing uncertainties in single-sample experiments, Mech. Eng. 75 (1) (1953) 3–8.
[32] Y.Y. Hsu, On the size range of active nucleation cavities on a heating surface, J. Heat Transfer 84 (1962) 207–216.
[33] V.P. Carey, Liquid–vapor phase-change phenomena, Taylor and Francis, 1992.
[34] S.W. Ruan, G. Bartsch, S.M. Yang, Characteristic of the critical heat flux for downward flow in a vertical tube at low flow rate and low pressure conditions, Exp. Therm. Fluid Sci. 7 (1993) 296–306.
[35] M. Ozawa, H. Umekawa, K. Mishima, T. Hibiki, Y. Saito, CHF in oscillatory flow boiling channels, Trans. IChemE (Part A) 79 (2001) 389–401.

[36] A.E. Bergles, S.G. Kandlikar, On the nature of critical heat flux in microchannels, J. Heat Transfer 127 (10) (2005) 101–107.
[37] A. Koşar, C.-J. Kuo, Y. Peles, Suppression of boiling flow oscillations in parallel microchannels with inlet restrictors, J. Heat Transfer 128 (3) (2006) 251–260.
[38] J.A. Boure, A.E. Bergles, L.S. Tong, Review of two-phase flow instability, Nucl. Eng. Des. 25 (1973) 165–192.